Nonlinear damping of high-power magnetostatic waves in yttrium–iron–garnet films

Mark M. Scott[a] and Carl E. Patton
Department of Physics, Colorado State University, Fort Collins, Colorado 80523

Mikhail P. Kostylev and Boris A. Kalinikos
St. Petersburg Electrotechnical University, St. Petersburg, 197376 Russian Federation

(Received 12 August 2003; accepted 17 February 2004)

The nonlinear decay of continuous-wave magnetostatic surface wave and backward volume wave signals has been measured for propagation in a narrow 6.9 μm thick yttrium–iron–garnet film strip, with excitation frequencies and wave numbers between 5470 and 5630 MHz and 47 and 216 rad/cm, respectively. The results show: (1) that the onset of nonlinear damping is a threshold effect, and (2) that a nonlinear decay model with two damping terms, one linear and one quadratic in the wave power, are needed to model the measured response. © *2004 American Institute of Physics.*
[DOI: 10.1063/1.1699503]

I. INTRODUCTION

The losses associated with high-power spin wave excitations in magnetic systems involve both linear and nonlinear decay processes. The nonlinear decay is primarily associated with the parametric generation of spin waves at high-power levels. Such processes were first treated in the pioneering work of Suhl and Schloemann on spin wave instability.[1,2]

More recently, there have been a number of studies on pulsed and continuous wave (cw) microwave excitations in ferrite films at high-power levels that demonstrate the generation of parametric spin waves.[3–6] Many of the related nonlinear wave phenomena of current interest involve parametric four-wave interaction processes. These processes can lead to a variety of effects in yttrium–iron–garnet (YIG) films such as self-modulational instability,[7–11] induced modulational instability,[12–15] decay instability,[16] and microwave magnetic envelope solitons.[17–19] The above experiments were carried out for a variety of magnetostatic wave (MSW) configurations and excitations in low loss single-crystal YIG films. Considered as a whole, these results provide a qualitative picture of the nonlinear spin waves produced under high-power pulse and cw excitation.

In spite of the above work, there have been no quantitative measurements or analyses of the increase in the damping rate of propagating MSW excitations at high-power levels. Furthermore, recent experimental and theoretical results on MSW soliton formation in YIG films through nonlinear mode beating indicate that nonlinear damping plays a critical role in this process.[16,20]

The present work was undertaken to provide a detailed and quantitative experimental and theoretical analysis of nonlinear damping for high-power MSW excitations. The specific objectives were threefold: (1) to use cw microwave excitations to generate high-power MSW signals in a YIG film delay line structure, (2) to measure the input–output power response profiles for these signals, and (3) to model the observed nonlinear response with a power dependent relaxation rate. The analysis shows that *two* nonlinear damping terms are needed to model accurately the measured response, one which scales with the power and the which scales with the square of the power.

Section II describes the MSW delay line structure and the measurement procedures. Section III presents input–output power response profiles for both surface and backward volume MSW configurations. Section IV summarizes the nonlinear damping model used for the analysis and gives example results and fits to the data. Section V provides a summary and conclusion.

II. DELAY LINE STRUCTURE, MEASUREMENT PROCEDURES, AND PARAMETERS

The experiments utilized a 6.9 μm thick low loss single-crystal YIG film strip in a two transducer MSW delay line structure.[7,18] The film strip was 3 cm long and 1.4 mm wide. The transducers consisted of narrow 50 μm wide, 2 mm long microstrip line sections grounded at one end and fed by standard 50 Ω microstrip lines.

Signals were detected in two ways. The output power data for the nonlinear damping analysis were obtained from the delay line output transducer. The low-power calibration data were obtained with an inductive probe technique.[21] The probe pick up section consisted of a small loop with a lateral size of about 200 μm made with 50 μm diameter wire. For MSW signal detection, the probe was scanned just above the surface of the film.

For all of the measurements described below, the applied in-plane magnetic field was set at 1260 Oe to position the low wave number MSW band edge frequency at 5590 MHz. This band edge frequency was selected to be high enough to eliminate complications at high power due to parametric spin waves at one-half of the pumping frequency.

Data were obtained for two in-plane field orientations, one with the field perpendicular and one parallel to the long

[a]Electronic mail: mark.scott@atk.com

edge of the YIG strip. For the perpendicular case, the propagating MSW signals along the strip correspond to magnetostatic surface wave (MSSW) excitations. For the parallel case, one has magnetostatic backward volume wave (MSBVW) excitations. For MSSW excitations, the frequency pass band lies above the band edge, while for MSBVW excitations the pass band is below the band edge.

The measurements for each orientation were carried out in three stages. In Stage I, the low-power dispersion curves of frequency ω versus wave number k were obtained. In Stage II, the low-power decay rates were determined. These data were obtained with the scanning probe.

Finally, in Stage III, the output versus input power response was measured for selected (ω,k) operating points on the dispersion curves for both types of MSW signals. These data were obtained over the full range of available power levels and yielded the nonlinear decay response. These Stage III data were obtained from measurements at the input and output transducers of the delay line for a transducer spacing L of 9 mm. Details on the analysis procedure are given below. The data are presented in Sec. III.

For the Stage I measurements, low-power cw power was applied simultaneously to both the input and the output transducers at the specified frequency and the scanning probe was used to measure the standing wave MSW signal amplitude as a function of position along the strip. Fits to these data gave the MSW wavelength and wave number in each case with good accuracy. These data were obtained over portions of the MSBVW and MSSW bands from 5590 to 5200 MHz and 5590 to 6100 MHz, respectively. Both of these ranges span wave numbers from approximately 10 to 1000 rad/cm. The decay data presented below cover only wave numbers up to approximately 200 rad/cm.

Fits to these data with the well-known Damon–Eshbach MSSW and MSBVW dispersion formulas[22] were used to set an empirical value for an effective saturation induction $4\pi M_{s\text{-eff}}$. With the known film thickness value S of 6.9 μm, the independent MSSW and MSBVW fits yielded a nominal $4\pi M_{s\text{-eff}}$ value of 1,900 G. It is likely that some part of this somewhat high $4\pi M_{s\text{-eff}}$ value, relative to the YIG textbook value of 1,750 G, is due to magnetocrystalline or stress-induced anisotropy. The dispersion curves were then used to obtain MSW group velocity $v_g(\omega)$ response functions for the two configurations.

In the Stage II measurements, further scanning probe data on the MSW signal spatial decay were obtained with microwave power applied to the input transducer only. For these measurements, the operating point frequencies for the MSSW and MSBVW configurations were set at 5650 MHz and 5540 MHz, respectively. The corresponding operating point wave numbers for these frequencies are about 74 rad/cm.

For each configuration, the low-power linear output probe signal level was measured as a function of input power for probe positions at 4 and 8 mm from the input. The relative separation Δz of 4 mm for the two positions was accurate to better than 0.1 μm. The slopes of the output versus input power linear response curves for the two probe points were then used to obtain the linear decay rate. With these slopes denoted by S_4 and S_8 for the 4 and 8 mm probe positions, respectively, the low-power temporal decay rate η_0 is given by $v_g \ln(S_4/S_8)/\Delta z$, where v_g corresponds to the empirical group velocity.

The above analysis gave a single η_0 value of $(4.4\times10^6\pm120)\ \mathrm{s}^{-1}$ that is consistent with the narrow ferromagnetic resonance linewidths found in low loss YIG films.[5] This means that for a frequency change from 5540 MHz to 5650 MHz, or one part in 60 or so, the maximum change in η_0 is less than about one part in 40,000. It is therefore reasonable to consider η_0 as frequency independent over the range of operating point (OP) frequencies in the Stage III measurements. This low-power relaxation rate will serve as a reference point for the high-power measurements.

In the Stage III measurements, transducer to transducer data on the output power as a function of the input power were obtained over the full range of input powers available, up to about 200 mW. The responses were notably nonlinear for input powers above about 2 mW. The data were obtained for four MSSW and MSBVW OP frequencies over the 5630–5710 MHz and 5570–5470 MHz bands, respectively. These data on the output *line* power P_{OL} as a function of the input *line* power P_{IL} were then used to determine: (1) a power dependent effective relaxation rate η_{eff} over the 9 mm propagation path and (2) the MSW power at the output transducer, P_{OMSW}, as a function of the MSW power at the input transducer, P_{IMSW}.

A nonlinear response for P_{IL} above about 2 mW means that the P_{OL} versus P_{IL} profiles should follow an equation of the form

$$P_{\mathrm{OL}}=AP_{\mathrm{IL}}e^{-2\eta_{\mathrm{eff}}L/v_g}, \tag{1}$$

where η_{eff} is power dependent and the parameter A is a combined electronic coupling coefficient for the input and output transducers. These electronic reductions are due to impedance mismatches and coupling losses. The A parameter is given by $\beta e^{2\eta_0 L/v_g}$, where β is the slope of the *linear* P_{OL} versus P_{IL} response for *low input power levels*. The empirical A values were frequency dependent. They were on the order of 0.1 for MSSW signals and 0.01 for MSBVW signals. Parameter values necessary for data analysis are listed in Tables I and II. Table I lists OP independent parameters. Unless otherwise indicated, a given parameter has the same nominal value for both the MSSW and the MSBVW configurations. Table II gives the four MSSW and MSBVW OP frequency and wave number values and the corresponding OP dependent group velocity and A values. In terms of the above parameters, the effective relaxation rate is given by

$$\eta_{\mathrm{eff}}=\frac{v_g}{2L}\ln\left(\frac{\beta}{P_{\mathrm{OL}}/P_{\mathrm{IL}}}\right)+\eta_0. \tag{2}$$

As the power increases into the nonlinear response regime and the $P_{\mathrm{OL}}/P_{\mathrm{IL}}$ ratio drops below β, η_{eff} moves above η_0. Note that *all parameters* here are accessible from experiment.

In order to extract the nonlinear MSW response within the film, one must analyze the P_{OL} versus P_{IL} data to obtain the P_{IMSW} and P_{OMSW} powers associated with the MSW sig-

TABLE I. Summary of thin film and delay line parameters.

Fitted effective saturation induction B_s	1900 G
Gyromagnetic constant γ	2.8 MHz/Oe
Film thickness S	6.9 μm
Film width W	1.4 mm
Transducer width w	50 μm
Transducer length ℓ	2 mm
Transducer separation L	9 mm
Nominal static applied magnetic field H	1260 Oe
Zero-wave number band edge frequency $\omega_B/2\pi$	5590 MHz
Low-power relaxation rate η_0	4.4×10^6 s^{-1}
Input line reflection coefficient Γ	0.156 (MSSW)
	0.528 (MSBVW)
Power amplitude to MSW power ratio $\lvert u\rvert^2/P_{\mathrm{IMSW}}$	1.384×10^{-4} l/mW (MSSW)
	2.086×10^{-4} l/mW (MSBVW)

nals at the input and output, respectively. A P_{OMSW} versus P_{IMSW} representation has two advantages. First, these MSW powers are independent of the details of the input and output coupling and, therefore, one may write a simple connection between P_{IMSW} and P_{OMSW} in terms of η_{eff}

$$P_{\mathrm{OMSW}}=P_{\mathrm{IMSW}}e^{-2\eta_{\mathrm{eff}}L/v_g}. \tag{3}$$

Second, these MSW powers can be related directly to the dynamic magnetization **m** at input and output. This conversion will prove to be important for the theoretical comparisons in Sec. V.

The input MSW power parameter P_{IMSW} is given by

$$P_{\mathrm{IMSW}}=F(1-\Gamma^2)P_{\mathrm{IL}}, \tag{4}$$

where F is a reciprocity/nonreciprocity factor and Γ denotes the voltage reflection coefficient at the mismatch between the input 50 Ω line and the input transducer. The F factor in Eq. (4) is equal to unity for nonreciprocal MSSW excitations and one-half for the reciprocal MSBVW signals. Based on standard MSW and microstrip analysis techniques, Stancil[23] has developed formulas for Γ as well as the connection between P_{IMSW} and the MSW dynamic magnetization amplitude. The working formulas are given in the Appendix.

The Stage III measurements were carried out for the four OP frequencies over the low wave number ends of the MSSW and MSBVW pass bands listed in Table II. For each point: (a) P_{OL} was obtained for P_{IL} values from about 0.005 mW to 200 mW. (b) The low power P_{OL} over P_{IL} ratio β and the relaxation rate parameter η_0 were used to determine the electronic reduction factor A. (c) The effective relaxation rate η_{eff} was then obtained as a function of P_{IL}. (d) P_{OMSW} versus P_{IMSW} profiles were obtained.

TABLE II. Tabulation of operating point specific parameters needed for the data analysis and theoretical comparisons.

Configuration	Frequency $\omega/2\pi$ (MHz)	Wave number k (rad/cm)	Group velocity v_g (cm/μs)	Electronic coupling coefficient $A\times10^{-3}$
MSSW	5630	47	5.107	69.556
	5650	72	4.916	78.077
	5670	99	4.719	74.186
	5710	154	4.344	122.229
MSBVW	5570	35	3.597	7.676
	5550	72	3.551	3.581
	5490	179	3.417	0.691
	5470	216	3.372	0.335

III. EXPERIMENTAL NONLINEAR DAMPING RESULTS

This section presents the Stage III results in three ways, (1) as plots of the measured P_{OL} versus P_{IL} profiles, (2) as plots of η_{eff} versus P_{IL}, and (3) as plots of P_{OMSW} versus P_{IMSW}. Each format provides its own particular perspective on the nonlinear response as a function of power.

Figure 1 shows representative P_{OL} versus P_{IL} results. The graphs in Figs. 1(a) and 1(b) show results for the MSSW and MSBVW configurations, respectively. The solid points show the data. The lines connecting the points are a guide for the eyes only. For each data set in Fig. 1(a), there are three response regions. For input powers below about 0.5 mW, the response is linear. For $0.5\,\mathrm{mW}<P_{\mathrm{IL}}<50\,\mathrm{mW}$ or so, there is a transition region in which the P_{OL} response gradually falls away from the low-power linear response. Finally, for $P_{\mathrm{IL}}>50\,\mathrm{mW}$, P_{OL} saturates at some fixed level that decreases with increasing wave number. Note that for the MSSW ge-

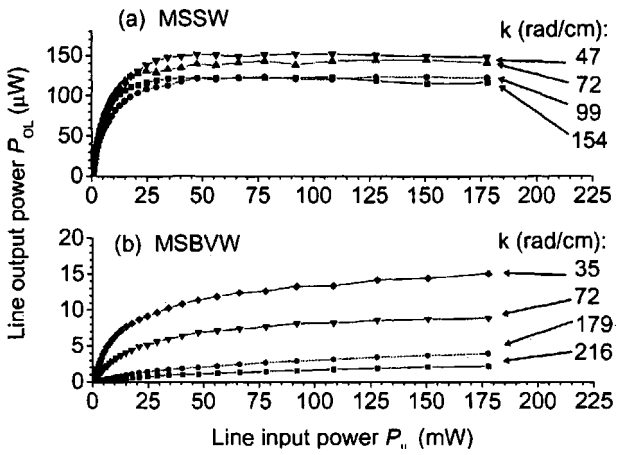

FIG. 1. (a) and (b) show the measured delay line output power P_{OL} as a function of the line input power P_{IL} for the MSSW and MSBVW configurations, respectively. The applicable operating point wave number k value for each data set is as indicated.

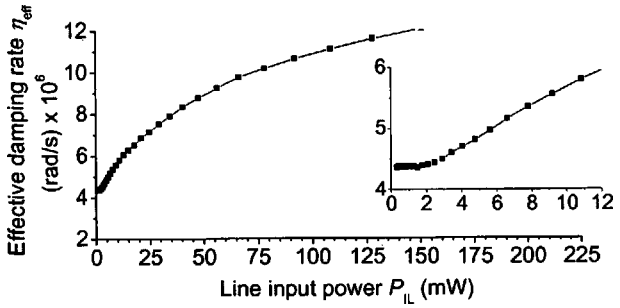

FIG. 2. Graph of the effective relaxation rate η_{eff} as a function of the line input power P_{IL}, as obtained from the data in Fig. 1(a) for $k=47$ rad/cm. The inset shows the response on an expanded scale.

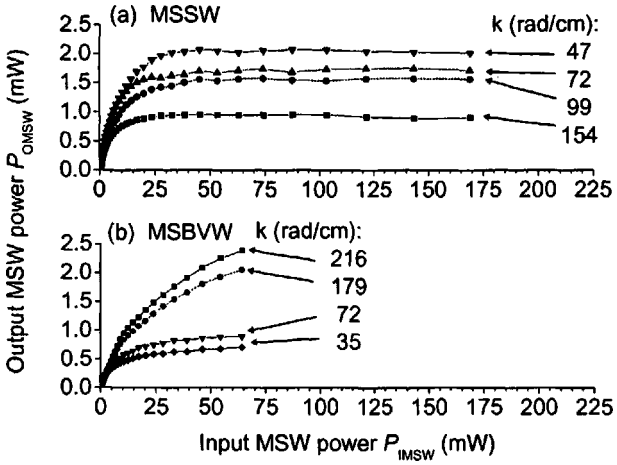

FIG. 3. (a) and (b) show the MSW output power P_{OMSW} as a function of the MSW input power P_{IMSW} for the MSSW and MSBVW configurations, respectively. The applicable signal wave number k for each data set is as indicated.

ometry, $(1-\Gamma^2)$ is about 0.98, and the actual P_{IMSW} input power is only 2% or so down from P_{IL}.

The data in Fig. 1(b) show a linear region at very low powers followed by a gradual fall off from the linear response for $P_{\text{IL}}>0.5$ mW or so, but saturation is not achieved at the highest powers. For the MSBVW configuration, $F(1-\Gamma^2)$ is about 0.36, so that the MSW input power P_{IMSW} into the film is down by 28% from the input line power. Because of this reduction, one cannot drive the MSBVW signal to the same nonlinear levels as obtained in the MSSW case.

At first glance, one might think that Fig. 1 shows a simple saturation effect. The η_{eff} results show, however, that the data are much richer than this. By way of example, Fig. 2 shows the extracted η_{eff} versus P_{IL} response for the $k=47$ rad/cm data from Fig. 1(a). Data are shown only for P_{IL} values above about 0.3 mW. Below this limit, a low level background signal at the output gives an anomalous $P_{\text{OL}}/P_{\text{IL}}$ ratio that almost doubles as P_{OL} drops down to the low-power limit of the actual measurements at 0.005 mW. The main graph shows the η_{eff} versus P_{IL} response with the same horizontal power scale as in Fig. 1(a). The inset shows the response on expanded horizontal and vertical scales.

The main graph shows the increase in the effective damping as the input power is increased from the low-power limit value at $\eta_{\text{eff}}=\eta_0$. As is evident from Eq. (2), the η_{eff} versus P_{IL} response will never saturate. The expanded scale data in the inset demonstrates the threshold nature of the nonlinear response, an aspect of the results not directly evident from the Fig. 1 data or the main graph in Fig. 2. While η_{eff} is constant at the low-power value for P_{IL} less than about 1.5 mW, there is a rather abrupt increase in the P_{IL} range from 1.5 to 2.5 mW.

The inset data demonstrate very clearly that the response here is more than a manifestation of saturation or limiter action. The fact that the relaxation rate sticks at the low-power level for a nonzero range of input power and then increases somewhat abruptly shows that this is an inherent nonlinear threshold process.

Figure 3 shows the entire ensemble of results on output MSW power P_{OMSW} versus input MSW power P_{IMSW} obtained from the line power data in Fig. 1. The displays follow the same format as Fig. 1; the top and bottom panels are for the MSSW and MSBVW configurations, respectively, and each panel shows response profiles for the appropriate OP frequencies in Table II.

The shapes of the MSW power profiles in Fig. 3 are similar to the line power profiles in Fig. 1, but with two critical differences. First, the data show that the ranges of P_{IMSW} values for the measurements of Figs. 3(a) and 3(b) are quite different. This follows from the very different values of the $F(1-\Gamma^2)$ values for the MSSW and MSBVW configurations discussed above. The ability to achieve saturation in the MSSW case proves to be quite useful. Section V will show that fits to the saturated MSSW data require the use of two nonlinear damping terms, one that scales with the instantaneous MSW power and one that scales with the square of this power. The lack of saturation in the MSBVW case precludes access to the second term.

Second, the ordering of the output power levels at the highest input powers for the different MSSW wave number operating points is preserved between Figs. 1(a) and 3(a), while it is inverted for the corresponding MSBVW results in the graphs of Figs. 1(b) and 3(b). This inversion is due primarily to the very weak dependence of the group velocity on wave number for the MSBVW excitations relative to the MSSW dependence.

IV. NONLINEAR DAMPING ANALYSIS

The key assumption for this section is that parametric spin wave processes are responsible for the nonlinear damping responses documented in Sec. III. Such processes are known to: (1) show a threshold effect and (2) commence at very low microwave powers for single crystal YIG materials. The results in Fig. 2 show these same characteristics. Measurements of the output power versus frequency spectra in the high-power saturation regime suggest that the primary mechanism responsible for nonlinear damping is a decay instability process.

The starting point for the analysis is the Landau-Ginzburg (LG) equation used extensively in nonlinear optics.[24] For the steady-state cw amplitude decay problem of

interest here, the LG formulation reduces to a simple nonlinear decay calculation. If only one damping term that scales linearly with the mode power is included, the problem can be solved analytically. If one includes both a linear term and one that scales with the square of the mode power, numerical solutions are required.

As already noted, it will prove convenient to work with a reduced amplitude parameter $u(z)$ in place of the line or MSW powers used in Sec. II. The u parameter convention used here follows Kalinikos and others.[25] In this convention, $u(z,t)$ is connected to the actual dynamic magnetization $\mathbf{m}(z,t)$ through the relation $u(z,t)=m(z,t)/\sqrt{2}M_s$. In the Kalinikos convention, m is a scalar complex magnetization amplitude for which $|m|^2$ is equal to the sum of the squares of the two components of **m** that are transverse to the static field. The M_s parameter denotes the saturation magnetization. Nonlinear effects usually come in for $|u|$—values and corresponding $|m|/M_s$ ratios in the 0.01 range. The u—parameter format makes it easy to see the relative size of the dynamic response compared to M_s. For the analysis below, m and u will be taken as real.

The cw nature of the experiments eliminates explicit time dependencies from the analysis. A steady-state spatial decay response is assumed. The calculations yield decay profiles of $u(z)$ versus z for given initial values of u at $z=0$. Evaluations of $u(z=L)=u_{\text{out}}$ as a function of $u(z=0)=u_{\text{in}}$ give response profiles that may be compared with the data

As stated above, Stancil[23] has given a detailed analysis of the calibration between the MSW power in the film and $|m|$. The Stancil formulas for this conversion are given in the Appendix. For the comparisons below, the P_{OMSW} versus P_{IMSW} data from Fig. 3 have been recast in a u_{out} versus u_{in} format based on these connections. For the parameters in Tables I and II and the formulas in the Appendix, the conversions from P_{IMSW} or P_{OMSW} to u_{in}^2 or u_{out}^2 are $1.38\times10^{-4}\,\text{mW}^{-1}$ for the MSSW configuration and $2.09\times10^{-4}\,\text{mW}^{-1}$ for the MSBVW case. These coefficients have a weak dependence on the operating point wave number at the 10^{-7} level that has been neglected.

For the present purposes, the LG equation may be written as

$$i\left(\frac{\partial u}{\partial t}+v_g\frac{\partial u}{\partial z}+\eta_0 u\right)+\frac{D}{2}\frac{\partial^2 u}{\partial z^2}-(N_1-i\nu_1)|u|^2u-(N_2-i\nu_2)|u|^4u=0. \tag{5}$$

The D parameter corresponds to the curvature of the MSW frequency ω versus wave number k dispersion evaluated at $|u|^2=0$ and the appropriate OP frequency. The N_1 and N_2 represent nonlinear frequency shift parameters given by the change in the mode frequency with respect to $|u|^2$ and $|u|^4$, respectively, also evaluated at the mode operating point. The ν_1 and ν_2 parameters represent the corresponding nonlinear damping coefficients. If η_0, ν_1, ν_2, and N_2 are set to zero, Eq. (5) matches the well-known nonlinear Schrödinger equation used extensively in nonlinear optics and nonlinear spin wave and MSW dynamics.

For a steady-state analysis, one may rewrite Eq. (5) as

$$\left[v_g\frac{\partial u}{\partial z}+(\eta_0+\nu_1|u|^2+\nu_2|u|^4)u\right]-i\left[\frac{D}{2}\frac{\partial^2 u}{\partial z^2}-N_1|u|^2u-N_2|u|^4u\right]=0. \tag{6}$$

The first square bracket term gives the decay for the reduced scalar amplitude $|u|$. The second square bracket term gives a nonlinear phase shift. While this phase shift is critical to the analysis of nonlinear pulse dynamics and solitons, for example, these terms have no effect on the decay response for cw excitation.

The term in parenthesis in Eq. (6) is the full amplitude dependent nonlinear relaxation rate

$$\eta(|u|)=\eta_0+\nu_1|u|^2+\nu_2|u|^4. \tag{7}$$

For cw signals, the instantaneous spatial decay rate $k_r(|u|)$ at a given amplitude is equal to $\eta(|u|)/v_g$. Without loss of generality, one may take u as real, write $\eta(u)=\eta_0+\nu_1u^2+\nu_2u^4$, and drop the second square bracket term in Eq. (6) entirely. One then obtains a simple equation for du, the change in the reduced amplitude u at position $z+dz$ in terms of the u—value at position z

$$du=-u[\eta_0+\nu_1u^2+\nu_2u^4](dz/v_g). \tag{8}$$

For low amplitude signals where $\nu_1u^2\ll\eta_0$ and $\nu_2u^4\ll\eta_0$, the decay response is exponential with a decay rate of η_0. For large amplitude signals, however, the decay is nonlinear and more rapid.

Without the ν_2u^4 term, Eq. (8) can be integrated to obtain an analytical expression for $u(z)$ given by

$$u(z)=\frac{u_{\text{in}}e^{-\eta_0 z/v_g}}{\sqrt{1+\nu_1u_{\text{in}}^2(1-e^{-\eta_0 z/v_g})/\eta_0}}. \tag{9}$$

If the ν_2u^4 term is included in Eq. (8), one obtains a transcendental equation for $u(z)$,

$$\frac{\eta_0 z}{v_g}=\ln\left(\frac{u_{\text{in}}}{u(z)}\right)+\frac{1}{4}\ln\left[\frac{\eta[u_{\text{in}}]}{\eta[u(z)]}\right]+\frac{\nu_1}{2G}\left(\tan^{-1}\frac{Q(u)}{G}-\tan^{-1}\frac{Q(u_{\text{in}})}{G}\right), \tag{10}$$

where $\eta[u]$ is defined through Eq. (7) with $|u|$ replaced by the now positive real u, G is equal to $(4\eta_0\nu_2-\nu_1^2)^{1/2}$, and $Q(u)$ is given by $\nu_1+2\nu_2u^2$.

Computed decay profiles of $u_{\text{out}}=u(L)$ versus u_{in} were obtained for parameters and conditions which match the values and operating points in Tables I and II. ν_1 and ν_2 were varied to yield best fits to power response profiles in Sec. III. For the MSSW geometry, the ability to go to high enough input powers to achieve output saturation made it possible to obtain best-fit values for both ν_1 and ν_2. For the MSBVW cases, the lack of a saturation response precluded any determinations for ν_2.

Figure 4 shows a series of representative u_{out} versus u_{in} computations and companion data that demonstrate the MSSW fitting procedure for the $k=47$ rad/cm operating point. The open circles show the data. The solid lines in Fig.

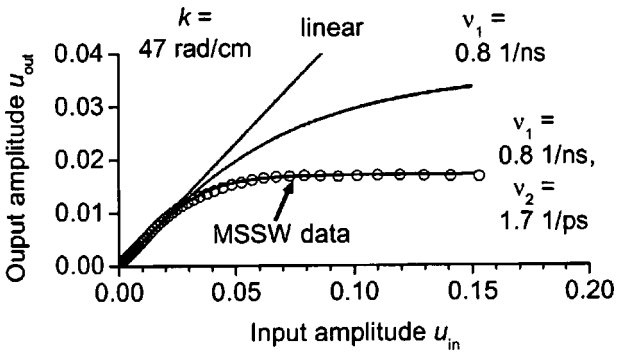

FIG. 4. Computed and experimental profiles of the reduced output amplitude u_{out} as a function of the reduced input amplitude u_{in} for the MSSW operating point at a wave number k of 47 rad/cm and other parameters as listed in Tables I and II. The solid curves show the linear response and nonlinear responses for values of the damping nonlinear damping coefficients ν_1 and ν_1, as indicated. The open circle points correspond to the data for $k=47$ rad/cm in Figs. 1 and 3 after conversion to the u_{out} versus u_{in} format.

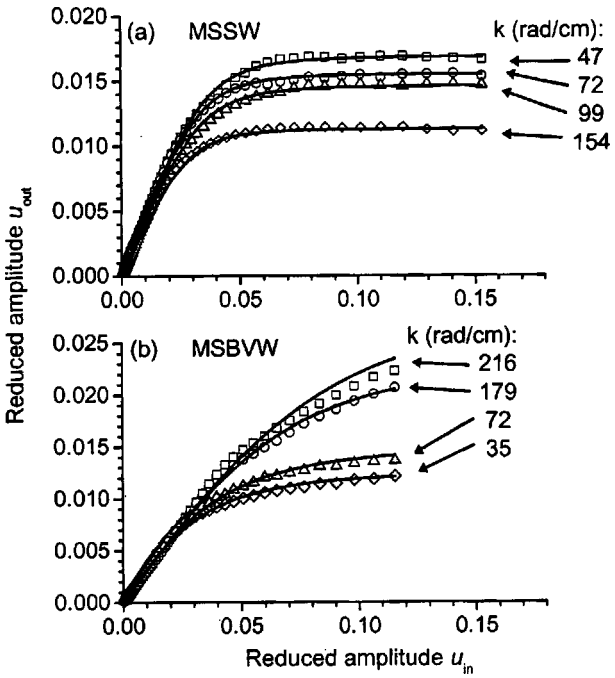

FIG. 5. (a) and (b) show the reduced output amplitude u_{out} as a function of the reduced input amplitude u_{in} for the MSSW and MSBVW configurations, respectively. The applicable signal wave number k for each data set is as indicated. The symbols show the data and the solid curves show best fits based on the nonlinear damping model.

4 show computed curves for the ν_1 and ν_2 values as indicated. The shape of the experimental response is different from those in Fig. 3 because the u amplitudes scale with the *square root* of the MSW powers. The linear response line in Fig. 4 is obtained when only the relaxation rate η_0 is included in the modeling. The rounded but nonsaturated curve shows a typical computed response if a nonzero ν_1 nonlinear term is included but the ν_2 parameter is set to zero. The saturated curve shows the result with both nonlinear terms included.

The fits to the data required a two-parameter optimization with careful attention to the shape of the bend-over region and the saturation levels. The curves in Fig. 4 demonstrate the main points. First, it is generally found that the use of the nonlinear ν_1 term alone cannot give a saturation response that matches the data and the bend over region at the same time. A ν_1 term alone can give a saturation at high values of u_{in}, but the resultant saturation u_{out}—values are then below those found experimentally and the bend over region matches poorly to the data. Moreover, such forced saturation requires very large values of ν_1. When both nonlinear terms are included, one can obtain reasonable fits for the bend over and the saturation regions for all of the MSSW data, with uncertainties in the optimum fit values of ν_1 and ν_2 of about ± 0.2 ns^{-1} and ± 0.2 ps^{-1}, respectively.

Figure 5 shows the same data as in Figs. 1 and 3 but recast in the u_{out} vs. u_{in} format of Fig. 4, along with best fits of the nonlinear response model to the data. The open symbols show the data and the solid lines show the fits. The format follows that of Figs. 1 and 3. The curves were obtained through numerical analysis based on Eq. (10), along with a one- or two-parameter best fit to the appropriate data. Table III lists the best fit ν_1 and ν_2 values as appropriate to the two configurations.

The u_{in} in Fig. 5 extend up to values of about 0.15 and 0.12 for the MSSW and the MSBVW cases, respectively. In both cases, the nonlinear responses set in for u_{in} values in the 0.03 range. In terms of u_{out}, the nonlinear responses all come in at values in the range of 0.01. This means that the nonlinear responses all occur for dynamic magnetization amplitudes that are about 1% of M_s.

As with the data in Fig. 4, the shapes of the curves in both graphs of Fig. 5 have a different appearance and scaling as compared to the results in Fig. 3. As noted, this is because the u amplitudes scale with the square root of the corresponding MSW powers. Because of this scaling, the initial responses in Fig. 5 have more of a linear appearance than the profiles in Fig. 3, the bend over extends out farther along the horizontal axis, and the region with a saturation response in Fig. 5(a) is reduced. The fits in Fig. 5 show that the nonlinear damping model provides a reasonable match to the data.

The listings in Table III demonstrate possible wave number dependences for the fitted nonlinear damping parameters. Keep in mind that the errors in the listed parameters from the fitting procedure given above are in the ± 0.2 ns^{-1} range for ν_1 and ± 0.2 ps^{-1} for ν_2. The trends shown in Table III are well beyond these error limits. The fits indicate that for

TABLE III. Tabulation of the nonlinear damping parameters ν_1 and ν_2 as obtained from best fits of the model to the data and listed as a function of increasing wave number k.

Wave number k (rad/cm)	MSSW ν_1 (1/ns)	MSSW ν_2 (1/ps)	MSBVW ν_1 (1/ns)
35	⋯	⋯	4.0
47	0.8	1.7	⋯
72	0.6	2.3	2.7
99	0.6	2.5	⋯
154	1.8	3.3	⋯
179	⋯	⋯	0.8
216	⋯	⋯	0.5

MSSW excitations, the ν_1 and ν_2 parameters both show an increase with wave number. For MSBVW excitations, in contrast, ν_1 appears to decreases with wave number.

It is important to keep in mind that, up until now, there is no fundamental theory for the ν_1 and ν_2 parameters. In the LG equation, these parameters are introduced simply as *ad hoc* imaginary parts for the first- and second-order nonlinear coefficients N_1 and N_2. Further experimental work is needed to quantitatively define the nonlinear damping parameters as a function of the MSW configuration, frequency, and wave number. It will also be critical to obtain a fundamental theory for the origin of these values.

V. CONCLUSIONS

Nonlinear damping for two types of cw MSW signals has been studied in a thin yttrium–iron–garnet film in the regime when parametric spin wave generation is allowed. First, the nonlinear MSW decay was measured and analyzed. Second, a phenomenological model was developed, based on the assumption that the nonlinear damping originates from parametric decay processes. Third, the nonlinear decay coefficients in the model were obtained from fits to the data. The model and the coefficients should prove useful for future work on nonlinear MSW propagation and decay. In this regard, recent experimental results on the simultaneous formation of bright and black solitons through the nonlinear mode beating of copropagating MSW signals can be described by this model.[16,20]

ACKNOWLEDGMENTS

This work was supported in part by the U.S. Army Research Office, Grant Nos. DAAG55-98-1-0430 and DAAD19-02-0197, the National Science Foundation, Grant No. DMR-0108797, the North Atlantic Treaty Organization Grant No. PST.CLG.978096, the Russian Foundation for Basic Research Grant No. 02-02-16485, and the International Association INTAS Grant No. 99-1812. Greg G. Boll, of GGB Industries, Inc., is acknowledged for the fabrication of the inductive probe.

APPENDIX

This appendix gives working expressions for: (1) the voltage reflection coefficient Γ introduced in Sec. II and (2) conversion from the MSW power P_{MSW} at any propagation point in the YIG strip, and the corresponding scalar dynamic magnetization amplitude m needed for the conversion from MSW power to the reduced amplitude u response in Sec. V. These expressions are derived from the microstrip line MSW coupling analysis by Stancil.[23] All expressions are given in *Systeme International* units.

For transmission lines in general, Γ is given by

$$\Gamma=\frac{R_r-R_g}{R_r+R_g}, \tag{A1}$$

where R_g is the impedance of the input line and R_r is the radiation resistance of the load. In the MSW setup used here, the input line is the microstrip input and R_g is 50 Ω and the load is the transducer element with the YIG film strip on top.

For the MSSW configuration, with the in-plane static field parallel to the transducer line element and perpendicular to the propagation direction along the YIG strip, R_r may be written as

$$R_r=\frac{\mu_0\omega l}{2kd}\left[\frac{1+\chi}{(1+\kappa)^2-(1+\chi)^2}\right]\left[J_0\left(\frac{kw}{2}\right)\right]^2, \tag{A2}$$

where μ_0 is the permeability of free space. The χ and κ are infinite medium susceptibility functions[22] given by $\chi=\omega_H\omega_M/(\omega_H^2-\omega^2)$ and $\kappa=\omega\omega_M/(\omega_H^2-\omega^2)$, where $\omega_H=|\gamma|H$ and $\omega_M=|\gamma|4\pi M_S$ specify the static in-plane field H and saturation magnetization M_S in frequency units.

For the MSBVW configuration with the in-plane static field along the propagation direction and perpendicular to the transducer line element, there is more than one possible mode. In the Stancil analysis,[23] the radiation resistance for this case is obtained for the lowest-order mode only. The final result may be written as

$$R_r=\frac{\mu_0\omega l\sin^2(\arctan(\beta))}{4\beta\arctan(\beta)}\left[J_0\left(\frac{\beta\arctan(\beta)w}{d}\right)\right]^2, \tag{A3}$$

with β equal to $[-(1+\chi)]^{1/2}$. Over the frequency range that supports MSBVW excitations in a film, β is real.

The connection between the MSW power P_{MSW} at a given point along the YIG strip and the dynamic magnetization amplitude m defined in Sec. IV may be obtained through a straightforward analysis of the MSW scalar potential. The Stancil result[23] involves averages over the direction normal to the film, taken as the y direction in the formulas below, to account for the spatial form of the MSW mode of interest. The m from the analysis represents, therefore, an average value over the film thickness.

For MSSW signals, the final $m-P_{\mathrm{MSW}}$ connection may be written as

$$m_{MSSW}=\sqrt{\frac{2P_{\mathrm{MSW}}k(\kappa^2+\chi^2)}{\beta^2\omega\alpha d\mu_0 W}}\times\int_{-d/2}^{d/2}\sqrt{(e^{2ky}+\alpha^2e^{-2ky})}dy. \tag{A4}$$

The α parameter denotes the function $\alpha(\omega,k)=(\chi-\kappa+2)e^{kd}/(\chi+\kappa)$. The χ and κ denote the same infinite medium susceptibility functions defined above. Over the range of wave numbers used for the MSSW measurements, the integral was approximately constant at 1.41. This value was used for the conversions in Sec. V.

The corresponding $m-P_{\mathrm{MSW}}$ connection for lowest-order mode MSBVW signals may be written in the form

$$m_{\mathrm{MSBVW}}=\sqrt{\frac{8P_{\mathrm{MSW}}\arctan(\beta)(\kappa^2+\chi^2)}{\omega d^2\mu_0 W}}\times\int_{-d/2}^{d/2}\cos\left(2\arctan\left(\beta\frac{y}{d}\right)\right)dy. \tag{A5}$$

Over the range of MSBVW wave numbers used for the measurements, the integral in Eq. (A5) was close to unity. This value was used for the conversions in Sec. V.

[1] H. Suhl, J. Phys. Solids **1**, 209 (1957).
[2] E. Schloemann, Ferromagnetic Resonance at High Power Levels, Technical Report R-48, Research Division, Raytheon Company, Waltham 54, MA, October 1, 1950.
[3] B. A. Kalinikos, N. G. Kovshikov, and N. V. Kozhus, Fiz. Tverd. Tela (Leningrad) **27**, 2794 (1985) [Sov. Phys. Solid State **27**, 1681 (1985)].
[4] W. D. Wilber, J. G. Booth, and C. E. Patton, J. Appl. Phys. **64**, 5477 (1988).
[5] M. Chen and C. E. Patton, in *Nonlinear Phenomena and Chaos in Magnetic Materials*, edited by P. E. Wigen (World Scientific, Singapore, 1994), pp. 33–82.
[6] H. Xia, P. Kabos, H. Y. Zhang, P. A. Kolodin, and C. E. Patton, Phys. Rev. Lett. **81**, 449 (1998).
[7] B. A. Kalinikos, N. G. Kovshikov, and A. N. Slavin, Zh. Eksp. Teor. Fiz. **94**, 159 (1988) [Sov. Phys. JETP **67**, 303 (1988)].
[8] P. E. Zil'berman, S. A. Nikitov, and A. G. Temiryazev, Pis'ma Zh. Eksp. Teor. Fiz. **42**, 92 (1985) [JETP Lett. **42**, 110 (1985)].
[9] S. Jun, S. A. Nikitov, R. Marcelli, and P. De Gasperis, J. Appl. Phys. **81**, 1341 (1996).
[10] C. S. Tsai, D. Young, and S. A. Nikitov, J. Appl. Phys. **84**, 1670 (1998).
[11] J. Su and C. S. Tsai, J. Appl. Phys. **87**, 1474 (2000).
[12] J. W. Boyle, S. A. Nikitov, A. D. Boardman, and K. Xie, J. Magn. Magn. Mater. **173**, 241 (1997).
[13] V. E. Demidov, Pis'ma Zh. Eksp. Teor. Fiz. **68**, 828 (2000) [JETP Lett. **68**, 869 (1998)].
[14] A. O. Korotkevich and S. A. Nikitov, Zh. Eksp. Teor. Fiz. **116**, 2058 (1999) [JETP **89**, 1114 (1999)].
[15] H. Benner, B. A. Kalinikos, N. G. Kovshikov, and M. P. Kostylev, Pis'ma Zh. Eksp. Teor. Fiz. **72**, 306 (2000) [JETP Lett. **72**, 213 (2000)].
[16] G. T. Kazakov, A. V. Kozhevnikov, and Y. U. Filimonov, Fiz. Tverd. Tela (Leningrad) **38**, 330 (1997) [Sov. Phys. Solid State **39**, 288 (1997)].
[17] M. Remoissenet, *Waves Called Solitons: Concepts and Experiments* (Springer, Berlin, 1999).
[18] C. E. Patton, P. Kabos, H. Xia, P. A. Kolodin, R. Staudinger, B. A. Kalinikos, and N. G. Kovshikov, J. Magn. Soc. Jpn. **23**, 605 (1999).
[19] A. N. Slavin, O. Buttner, M. Bauer, S. O. Demokritov, B. Hillebrands, M. M. Kostylev, B. A. Kalinikos, V. V. Grimalsky, and Y. Rapoport, Chaos **13**, 693 (2003).
[20] M. M. Scott, B. A. Kalinikos, and C. E. Patton, *Digest for the International Magnetics Conference*, Digest HD-04, Boston, MA (2003 Mira CD-Rom Digital Publishing, Inc. St. Louis, MO).
[21] M. M. Scott, B. A. Kalinikos, and C. E. Patton, J. Appl. Phys. **94**, 5877 (2003).
[22] R. W. Damon and J. Eshbach, J. Phys. Chem. Solids **19**, 308 (1961).
[23] D. D. Stancil, *Theory of Magnetostatic Waves* (Springer, New York, 1993).
[24] G. P. Agrawal, *Nonlinear Fiber Optics* (Academic, San Diego, 1995).
[25] B. A. Kalinikos, N. G. Kovshikov, and A. N. Slavin, J. Appl. Phys. **69**, 5712 (1991).